Interferometric imaging for the tomography of rough particles in a flow: A case study

Marc Brunel, Barbara Delestre, Mohamed Talbi, Michael Fromager

Version of Record: https://www.sciencedirect.com/science/article/pii/S0030401820308294
Manuscript_77c86ac7b5a4023a039805408679a6b5

Interferometric imaging for the tomography of rough particles in a flow : a case study

Marc Brunel[1,*], Barbara Delestre[1], Mohamed Talbi[1], Michael Fromager[2]

[1]*UMR CNRS 6614 CORIA, Université de Rouen Normandie, Avenue de l'Université, BP 12, 76801 Saint-Etienne du Rouvray Cedex, France*
[2]*UMR CNRS 6252 CIMAP, CEA, Ensicaen, Université de Caen, 6 Bd Maréchal Juin, F-14050 Caen Cedex, France*
**marc.brunel@coria.fr*

Abstract

The possibility to perform the tomography of irregularly-shaped rough particles in a flow using multi-view interferometric imaging is investigated. Combining three perpendicular angles of views, we reconstruct a family of possible 3D-shapes from speckle patterns. The estimation of an error parameter enables the elimination of erroneous 3D-shapes to obtain a more accurate estimation of the particle's volume. The principle is tested and confirmed experimentally by analysing a set of three interferometric images of "programmable" particles generated by a digital micromirror device.

I - Introduction

The tomography of irregularly-shaped particles in a flow is particularily interesting for meteorology, combustion, nuclear safety and any domain concerned. In many cases, a single-shot technique is necessary because the speed of particles can be very important, and instruments should tend ideally to a real-time analysis. A configuration as the CT-scan (computed tomography scan) in medicine where the object is fixed while the x-ray tube rotates around the object is not applicable. In a similar way, other methods as confocal microscopy, electron, or optical tomographic microscopy require fixing, trapping or confining particles [1-5]. In airborne operation or in icing wind tunnels for example, the relative speed of particles as ice crystals or ashes due to the plane's flight can exceed 200ms^{-1}. A setup where the particle is illuminated by a unique short flash, while different sensors acquire simultaneously the signal delivered by the particle in different directions, must be envisaged. Light scattering techniques are good candidates because they can answer these requirements, and first set-ups have been developed, using digital holography for example [6].
In this family of techniques based on light scattering properties, interferometric particle imaging appears as another interesting candidate [7]. When illuminated by a laser pulse, rough particles generate interferometric images that are speckle patterns. They can be linked quantitatively in size and shape with the initial shape of the particle [8-14]. Dual-view set-ups have been tested to make simple 3D-particle's shape recognition, or to estimate the volume of ice particles in a flow [7,9,12]. But set-ups proposing three perpendicular angles of view to give a more-complete description of the particle have not been done yet. One difficulty arises from the analysis of the interferometric images of the particles. After 2D-Fourier transformation, these images give the 2D-autocorrelation of the contour of the particle projected in the plane of the CCD sensor (corresponding to this angle of view). As the 2D-autocorrelation of a 2D-shape is not the 2D-shape itself, the reconstruction procedure combining different views can be particularly complex. It is the aim of this study to realize a case

study in order to understand the difficulties that can appear from the combination of three views from three perpendicular angles of view.

Section II will describe the principle of the case study carried out in this article. Section III will then describe the experimental set-up used to record the interferometric images of « programmable » rough particles. It uses a Digital Micromirror Device (DMD) [15,16]. The interferometric images of a « programmable » particle, observed from three perpendicular angles of view, will be presented and analyzed. Section IV will propose 2D-reconstructions of the three faces of the particle, while 3D-reconstructions combining the three perpendicular angles of view will be realized in section V. This section will show how a reconstruction's error parameter can be defined, how it can be used to refine the particle's shape reconstruction and to reduce the uncertainty about the particle's volume combining the three views. Section VI will investigate the possibility to generalize the conclusions to other cases.

II - Principle of the case study

Interferometric Particle Imaging (IPI) enables rough particle sizing. First developed to measure the size of spherical droplets or bubbles, it could be extended to the analysis of irregularly-shaped rough particles. Let us consider an irregular rough particle under coherent laser illumination. There is no theoretical model to predict rigorously the filed scattered by the particle. Using a simplified description, the rough particle can be assimilated to an ensemble of coherent point emitters that cover the whole particle. With a scalar Huygens-Fresnel model, the 2 dimensional Fourier transform of the interferometric image of the particle is then shown to be linked to the 2D-autocorrelation of the envelope of the particle through relation (1) :

$$|FT_{2D}[I](\lambda B_{tot}u, \lambda B_{tot}v)| \propto |A_{2D}[G_0](dx, dy)| \qquad (1)$$

where *I* is the intensity of the interferometric out-of-focus image of the particle and G_0 the electric field scattered by the illuminated particle (a sum of Dirac functions representing each point emitter). λ is the wavelength of the laser. λB_{tot} is the scaling factor between both functions which is deduced from the set-up. The correspondence between these two functions has been validated in size and shape in many cases, and reproduced with "programmable" particles generated with a Digital Micromirrors Device (DMD) [7-12,14-16].

The relation (1) indicates that the shape of a rough particle, under coherent laser illumination, can be studied from the analysis of its interferometric image. This property has been validated in many cases using single-view setups. The extension of these methods to multi-view systems is particularly attractive to perform the tomography of irregular rough particles in a flow. This paper presents a case study to confirm this potentiality of multi-view IPI, identify some problems and their possible solutions.

Figure 1 shows the principle of the configuration that will be considered in this article. Three IPI systems (composed of an objective, an extension tube and a CCD sensor) visualize a region of interest from three orthogonal directions. The aim of our study is to evaluate the potentiality of this set-up when analysing simultaneously the three images delivered by the three views, and specifically:

- the possibility to reconstruct approximately the 3D-shape and the orientation of a transparent or translucent rough particle in the flow.
- the possibility to measure the volume of the particle as precisely as possible

Figure 1 details the orientation of the different axes that will be used in the study for a better understanding of all results.

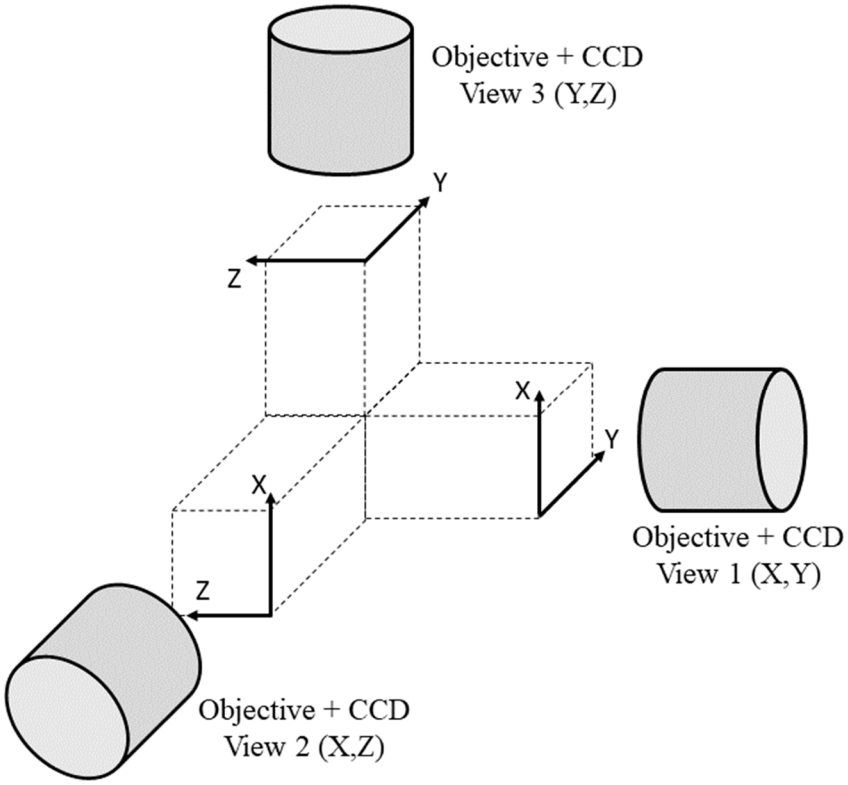

Fig. 1 : schematic configuration of a 3-views interferometric imaging setup

III – Experimental set-up and image acquisition

Unfortunately, it is not not possible experimentally to know perfectly the exact orientation of a rough particle in a flow. We can eventually know the exact shape of the particle that is injected into a flow but we are not able to predict its exact orientation when it reaches the region of interest of the imaging set-up. It is thus not possible to perform rigorous experiments where the rough particles are perfectly known (size, shape and orientation). It brings an important limitation to the goal of our study. We have thus decided to record the interferometric images of perfectly known « programmable » particles. The real set-up used in this study is composed of a Digital Micromirror Device (DMD) that reproduces a « programmed rough particle » illuminated by an HeNe laser (wavelength: 632.8 nm). It is presented in figure 2. The particle is composed of the micromirrors that are programmed « on-state », i.e. that reflect the laser light into the direction of an imaging system. Other micromirrors keep « off-state » : i.e. no reflection in the direction of the imaging system. This imaging system is composed of a lens and a CCD sensor. The CCD sensors records the out-of-focus image of the particle programmed on the DMD, which is a speckle pattern.

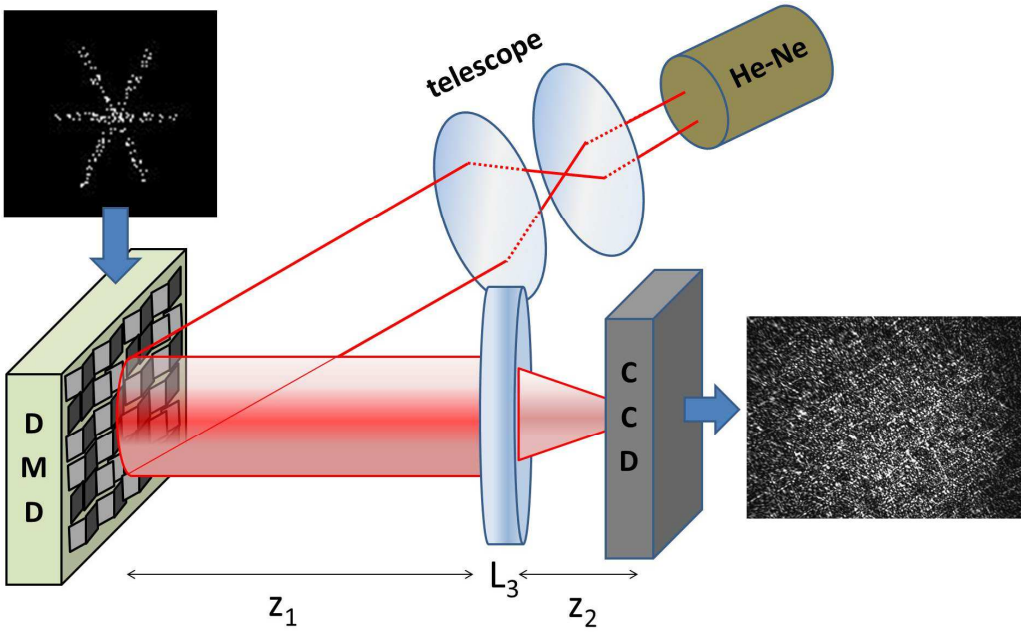

Fig. 2 : experimental set up to generate the interferometric images of « programmable » particles with a Digital Micromirror Device.

Let us now explain the procedure used to reproduce virtually the experiment of figure 1 with a perfectly known rough particle in the region of interest. The 3D-shape of the particle to be reproduced with the DMD is depicted in perspective on figure 3. It looks like an irregular stick-like particle, without any axis of symmetry. The detail of the three views is given in figure 4 :

- View 1 shows the shape of the projection of the particle in the (X,Y) plane. It is represented in figure 4(a). From this angle of view, the particle is programmed as an ensemble of 461 on-state micromirrors that cover the envelope of the particle according to this view. The on-state mirrors are the bright spots on the figure.
- View 2 shows the shape of the projection of the particle in the (X,Z) plane. It is represented in figure 4(b). From this angle of view, the particle is programmed as an ensemble of 1222 on-state micromirrors that cover the envelope of the particle according to this view.
- View 3 shows the shape of the projection of the particle in the (Y,Z) plane. It is represented in figure 4(c). From this angle of view, the particle is programmed as an ensemble of 1788 on-state micromirrors that cover the envelope of the particle according to this view.

We have avoided to reproduce a smooth ovoidal particle because the possible 2D-shapes delivered for reconstruction would be very similar, and the conclusions would not be very instructive. The DMD active screen used is the model DLP6500FYEHD by Texas Instruments. It has full HD resolution 1080 p (1920 × 1080 mirrors with a square geometry). The separation between the centers of two adjacent mirrors is 7.56 µm. Each pixel on figure 4 has thus a dimension of $7.56\mu m \times 7.56\mu m$.

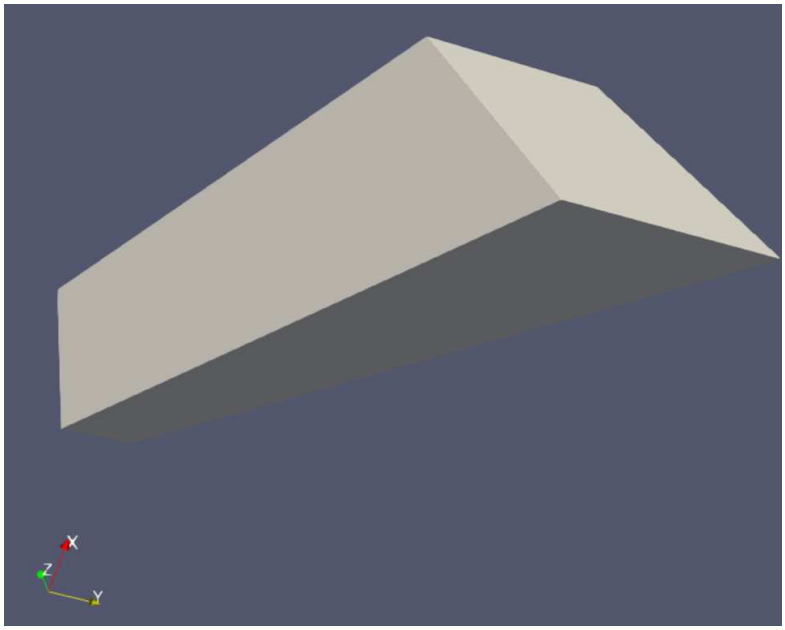

Fig. 3 : 3D-shape of the particle under study

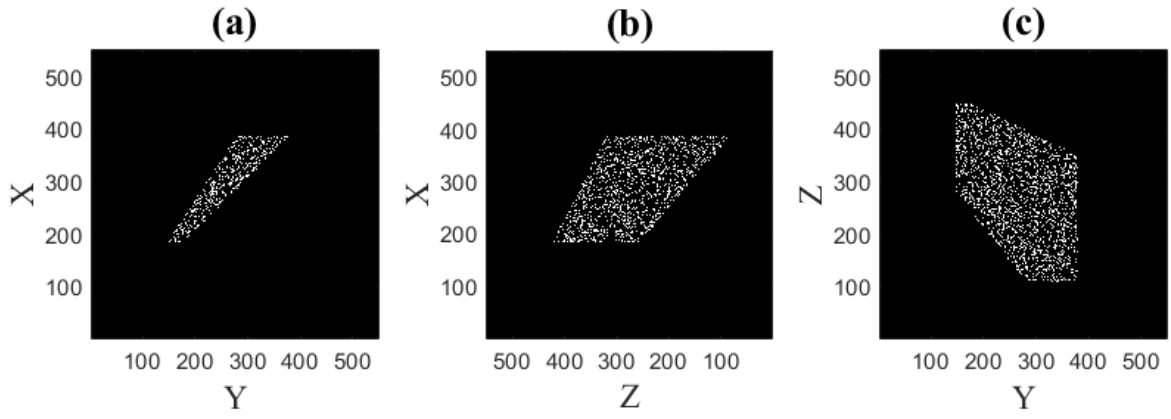

Fig. 4 : The three orthogonal projections of the particle under study in the plane (X,Y) (Fig. (a)), (X,Z) (Fig. (b)) and (Y,Z) (Fig. (c)). Axes are in pixels. The pixel size is $7.56\mu m \times 7.56\mu m$.

Let us now discuss the experimental interferometric images obtained for the virtual object described in figures 3 and 4. The imaging system is in the direction associated to the "On-State" micro-mirrors. It includes a converging lens L_3 (focus length *f= 50 mm*) and a CCD sensor. This sensor is a Thorlabs BC106N-VIS/M camera with 1360 x 1024 pixels, and a pixel size of $6.45\mu m \times 6.45\mu m$. The first facet programmed on the DMD is the one of figure 4(a) corresponding to the projection of the rough particle on the (X,Y)-plane. The interferometric image $I_{view\,1}(x, y)$ recorded on the CCD sensor is reported on figure 5(a). Axes are in pixels. Each pixel of figure 5(a) has the dimension of the pixel size of the CCD sensor, i.e. $6.45\mu m$. This interferometric image $I_{view\,1}(x, y)$ is 2D-Fourier transformed. Figure 5(b) shows $log\big(FT_{2D}[I_{view\,1}(x, y)](\lambda B_{tot}u, \lambda B_{tot}v)\big)$. (u, v) are the conjugated coordinates of (x, y) in the Fourier domain. λB_{tot} is the scaling factor previously mentionned in equation (1).

Quantitatively, the coefficient B_{tot} equals 0.079m. Note that the CCD sensor is not perfectly parallel to the plane of the DMD. It means that the B_{tot} coefficient could be slightly different from one

micromirror to another one. Nevertheless, the defocus parameter is high which induces a high value of B_{tot} in the configuration of the paper. This effect is thus negligible here and has no impact on the results.

The interferometric images that are Fourier transformed are composed of 700×700 pixels of height $6.45\mu m$. After 2D-Fourier-transformation, the resulting images (the 2D-FFT) are resized to 250×250 pixels to reduce the future reconstruction time. After these different steps and application of the scaling factor λB_{tot}, the pixel size in figure 5(b) is $31.4\mu m$. Figure 5(c) shows finally $log\big(FT_{2D}[I_{view\,1}(x,y)](\lambda B_{tot}u, \lambda B_{tot}v)\big)$ after binarization. The pixel size is the same as in previous figure 5(b).

In a similar way, the second facet programmed on the DMD is the one of figure 4(b) corresponding to the projection of the rough particle on the (X,Z)-plane. The interferometric image $I_{view\,2}(x,z)$ recorded on the CCD sensor is reported on figure 6(a) (Axes are in pixels of $6.45\mu m$ height). This interferometric image $I_{view\,2}(x,z)$ is 2D-Fourier transformed. After resizing of the resulting images and application of the scaling factor, figure 6(b) shows $log\big(FT_{2D}[I_{view\,2}(x,z)](\lambda B_{tot}u, \lambda B_{tot}w)\big)$. w is the conjugated coordinate of z in the Fourier domain. As for figure 5(b), the pixel size in figure 6(b) is $31.4\mu m$. Figure 6(c) shows finally $log\big(FT_{2D}[I_{view\,2}(x,z)](\lambda B_{tot}u, \lambda B_{tot}w)\big)$ after binarization (same pixel size as in figure 6(b)).

Finally, the third facet programmed on the DMD is the one of figure 4(c) corresponding to the projection of the rough particle on the (Y,Z)-plane. The interferometric image $I_{view\,3}(y,z)$ recorded on the CCD sensor is reported on figure 7(a) (Axes in pixels of $6.45\mu m$). This interferometric image $I_{view\,3}(y,z)$ is 2D-Fourier transformed. Figure 5(b) shows $log\big(FT_{2D}[I_{view\,3}(y,z)](\lambda B_{tot}v, \lambda B_{tot}w)\big)$. (pixel size in Fig. 7(b) of $31.4\mu m$) . Figure 7(c) shows finally $log\big(FT_{2D}[I_{view\,3}(y,z)](\lambda B_{tot}v, \lambda B_{tot}w)\big)$ after binarization (same pixel size as in figure 7(b)).

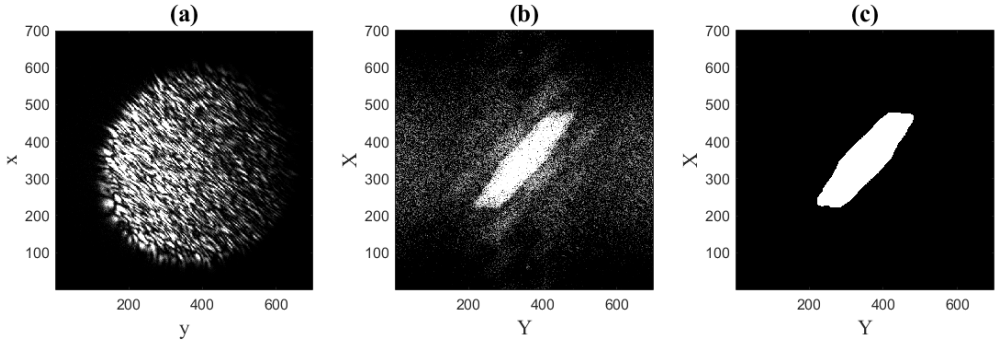

Fig. 5 : interferometric image of face presented in Fig. 4(a) (a), the logarithm of its 2D-Fourier transform (b), and the binarized 2D-Fourier transform of the interferometric pattern (c).

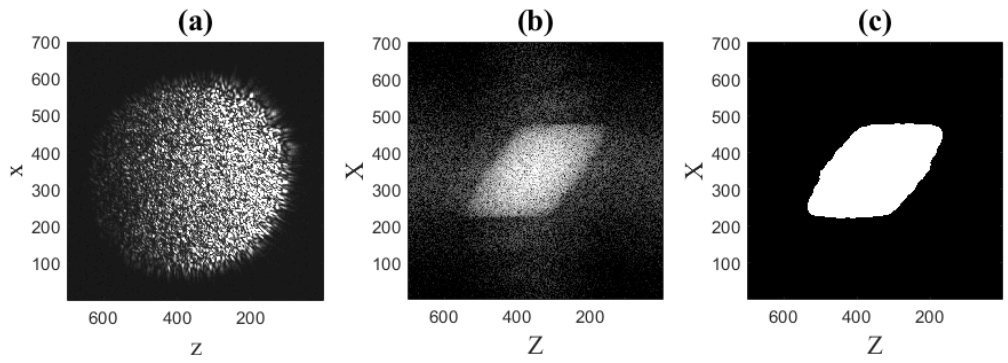

Fig. 6 : interferometric image of face presented in Fig. 4(b) (a), the logarithm of its 2D-Fourier transform (b), and the binarized 2D-Fourier transform of the interferometric pattern (c)

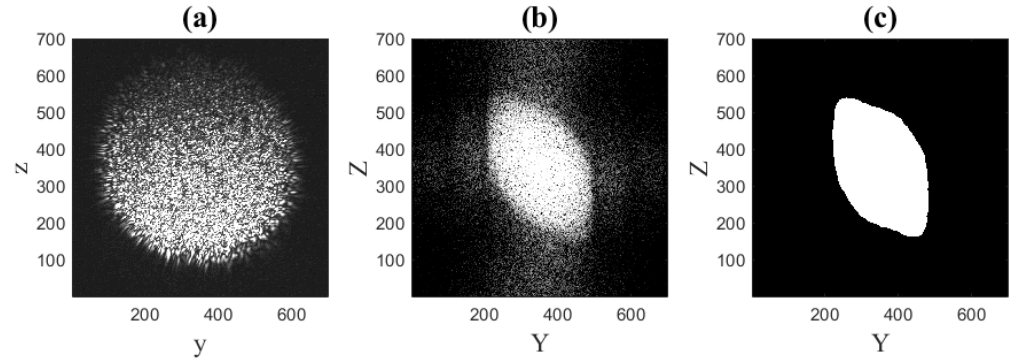

Fig. 7 : interferometric image of face presented in Fig. 4(c) (a), the logarithm of its 2D-Fourier transform (b), and the binarized 2D-Fourier transform of the interferometric pattern (c)

IV- 2D-reconstructions, view by view

According to the simplified expression (1), the binarized Fourier transform of the first speckle pattern (Fig. 5(a)) presented in Fig. 5(c) reproduces very well the 2D-autocorrelation of the contour of the object's facet of figure 4(a). The same property can be observed from Fig. 6(c) associated to the facet of figure 4(b), and from Fig. 7(c) associated to the facet of figure 4(c). There is actually just a significant difference : the sharp extremities of the particle's facets should induce sharp extremities on the binarized Fourier transforms of the speckle patterns. Unfortunately, these sharp extremities are lost during the binarization process, due to the low signal obtained at these extremities on figure 5(b), 6(b) and 7(b) respectively. A simple explanation can be given ; the facets are composed of a few emitters only (« on-state » micro-mirrors) in the extremities. These micromirrors contribute thus slightly to the formation of the speckle patterns, bringing barely more signal than noise. It is thus expected to reconstruct objects with extremities more curved than the initial real objects.

Let us now realize some 2D-reconstructions of the different facets from their speckle patterns. Based on relation (1), the numerical values of both functions $|FT_{2D}[I](\lambda\, \mathrm{B}_{tot}\, u, \lambda\, \mathrm{B}_{tot}\, v)|$ and $|A_{2D}[G_0](dx, dy)|$ could be compared in any point $(\lambda\, \mathrm{B}_{tot}\, u, \lambda\, \mathrm{B}_{tot}\, v)$ and (dx,dy) respectively. Algorithms enable indeed the reconstruction of the support of a 2D-object from its 2D-

autocorrelation. Reconstructions of the different facets should thus be possible from their corresponding speckle patterns. Unfortunately, the validation of relation (1) has been limited experimentally to the comparison of the contours of both binarized functions. A deeper correspondence has not been demonstrated experimentally yet. We are thus limited to the proposition of families of 2D-shapes whose contour of their 2D-autocorrelation match the contour of the 2D-Fourier transform of the speckle patterns that they produce.

We recall first briefly the tri-intersection method that can be used to do this [17,7]. We consider a centrosymmetric 2D-shape noted A (it is the initial 2D-autocorrelation). It is duplicated twice. Both copies are translated adequately from vectors $\boldsymbol{\omega_1}$ and $\boldsymbol{\omega_2}$. The tri-intersection B of the initial shape A with the two translated copies (A+ ω_1) and (A+ ω_2) (i.e. B=A∩(A+ ω_1))∩(A+ ω_2)) gives then a possible 2D-object B whose 2D-autocorrelation matches the initial one A. The choice of vectors $\boldsymbol{\omega_1}$ and $\boldsymbol{\omega_2}$ leads to a family of possible objects. Based on this method, we have developed a program that delivers possible 2D-shapes whose 2D-autocorrelation match the contour of the 2D-Fourier transform of any interferometric pattern recorded experimentally. It is first applied to figure 5(c). Figure 8 shows three possible facets whose 2D-autocorrelation gives the one of figure 5(c). The pixel size on figure 8 is the same as on figure 5(c), i.e. $31.4\mu m$ per pixel. It is interesting to note that the 2D-shape (A1) is very similar qualitatively and quantitatively (exact size) to the original contour that has been programmed on the DMD (see the contour of all « on-state mirrors » on figure 4(a)). (A3) is the centrosymmetric shape that has a similar 2D-autocorrelation, while shape (A2) is an intermediate solution between shapes (A1) and (A3). As previously mentioned, some extremities are in general not so sharp as the original programmed object.

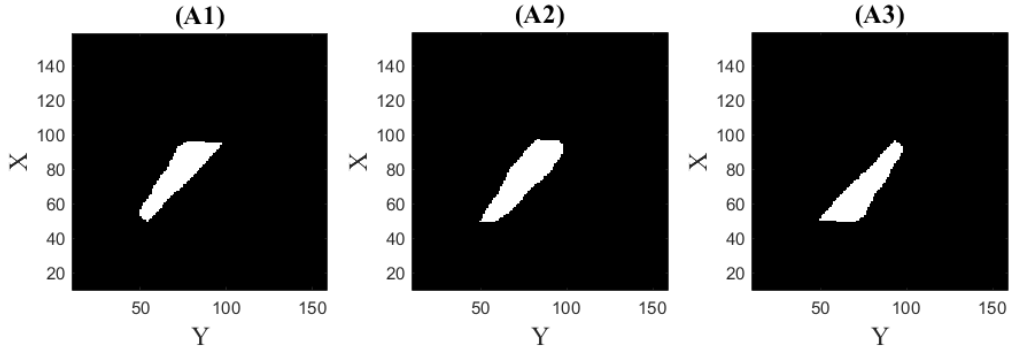

Fig. 8 : three possible 2D-shapes whose 2D-autocorrelation matches Fig. 5(c) ($31.4\mu m$ per pixel).

In a similar way figure 9 shows three possible facets whose 2D-autocorrelation gives the one of figure 6(c). The pixel size is the same. The 2D-shape (B1) looks like the original contour that has been programmed on the DMD (see the contour of all « on-state mirrors » on figure 4(b)), although some extermities are not so sharp. (B3) is the centrosymmetric shape of (B1), while shape (B2) is an intermediate solution between shapes (B1) and (B3).

The third view presented in figure 4(c) is slightly more complex. We thus present more possible shapes whose 2D-autocorrelations give the one of figure 7(c). Figure 10 shows six possible shapes called (C1) to (C6). The pixel size is the same as in figures 7(c), 8 and 9. The 2D-shape (C1) is the most resembling shape to the original view of figure 4(c). (C6) is the centrosymmetric shape of (C1). Other shapes show a family of intermediate solutions from (C1) to (C6).

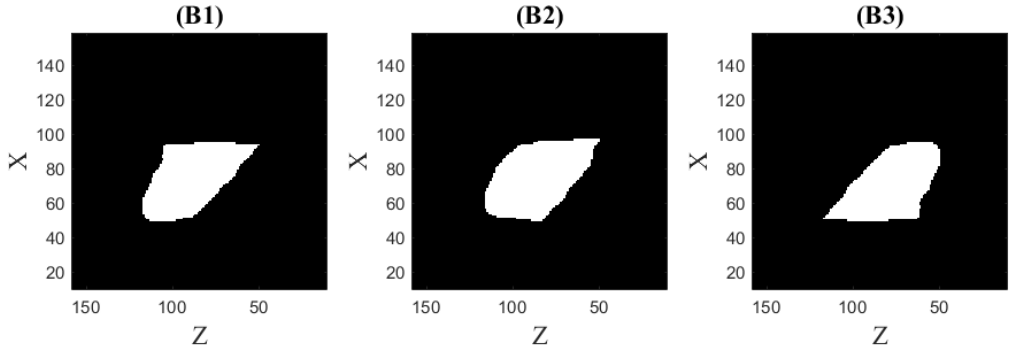

Fig. 9 : three possible 2D-shapes whose 2D-autocorrelations match Fig. 6(c) ($31.4\mu m$ per pixel).

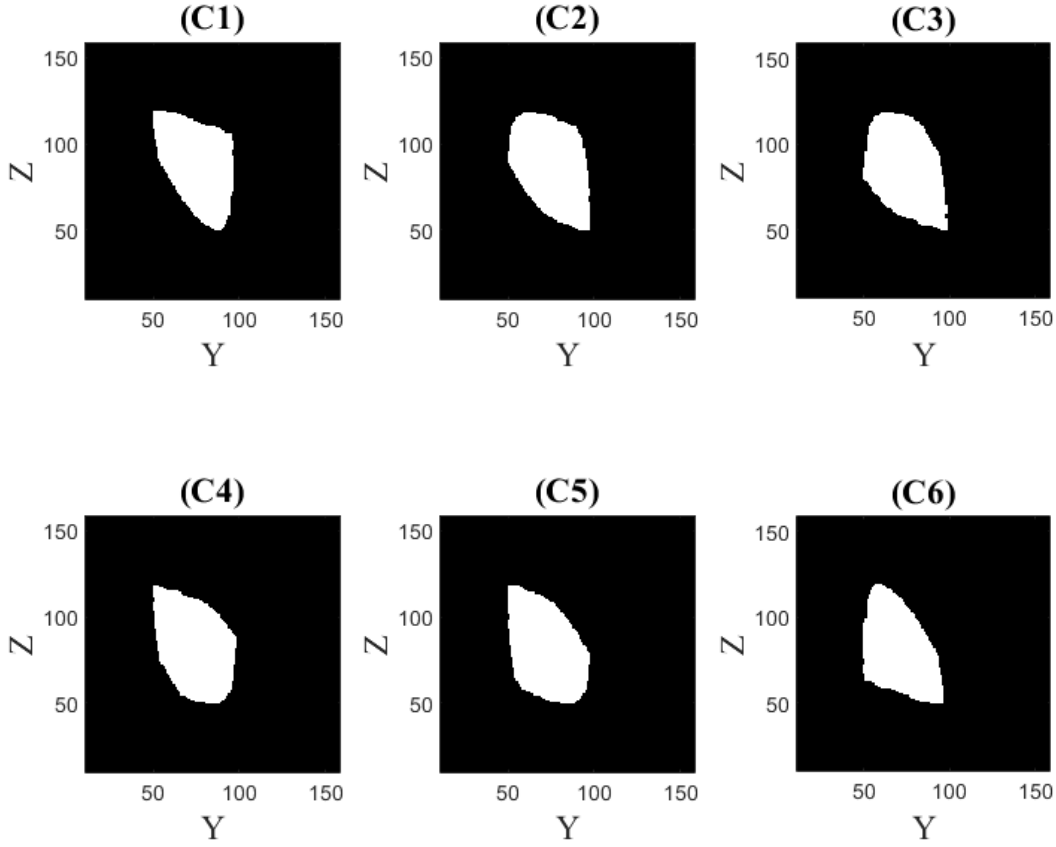

Fig. 10 : six possible 2D-shapes whose 2D-autocorrelation matches Fig. 7(c) ($31.4\mu m$ per pixel).

V – 3D-reconstructions

In classical tomography, the quality of the 3D-reconstruction of an object requires a high number of angles of view. The quality of the 3D-reconstruction of an object using only three perpendicular angles of view should be very limited here. In addition, the principle of a 3D-reconstruction is very

challenging in the case of interferometric particle imaging because different 2D-shapes can exhibit similar 2D-autocorrelations, as previously detailed. It is intriguing to identify the conclusions that can be drawn using the configuration of figure 1 in terms of simplified tomography of particles in a flow. Using only two perpendicular angles of view, it is possible to realize a simplified reconstruction as illustrated on figure 11. Mask 1 represents one possible shape in the (X,Y)-plane while mask 2 represents one possible shape in the (X,Z)-plane. If both masks are a square and a circle respectively, a cylinder is reconstructed in this case. There is no incompatibility between both views when processing like this, except that the size of aperture of the two masks 1 and 2 must be the same along the X-direction that is common to both views. Let us now add a mask 3 corresponding to the knowledge of a possible shape along the (Y,Z)-plane. We add then a third projection to build more precisely the 3D-shape of the particle. The presence of three views can lead to an incompatibility between views. The combination of three projections to reconstruct the 3D-object from three masks can indeed lead to a final object whose projection along the three planes (X,Y), (X,Z) and (Y,Z) does not match the three initial masks anymore. Some parts of the object expected by the shape of mask 1 can finally have been suppressed by the projection process linked to the shapes of masks 2 and 3 for example.

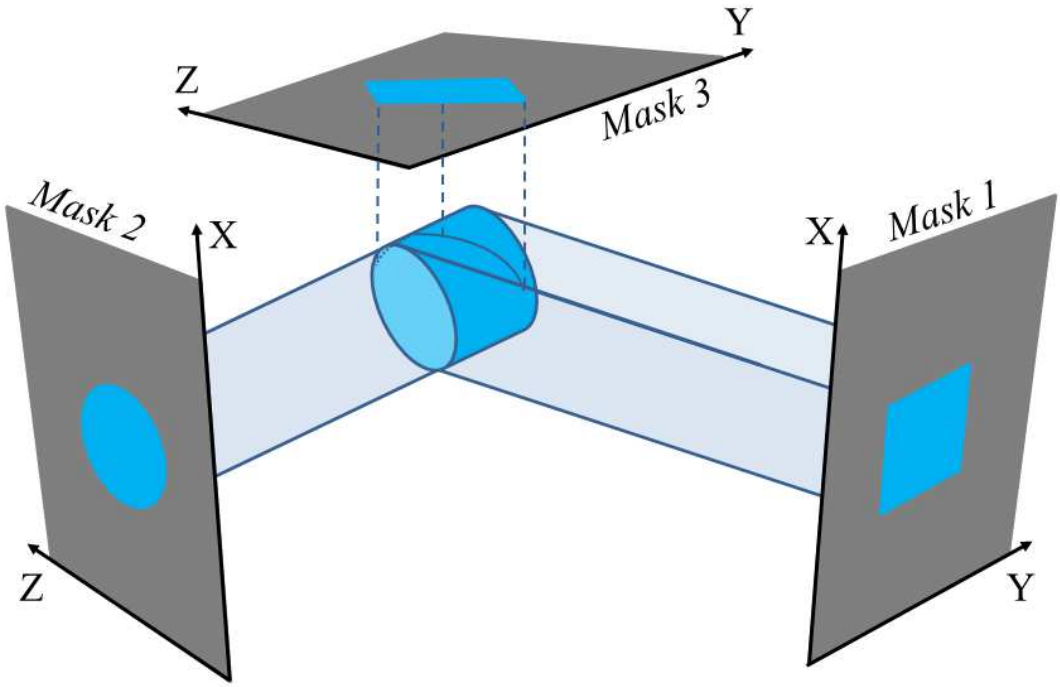

Fig. 11 : schematic representation of the principle of 3D-reconstruction from three perpendicular views (mask 3 is not the good one in this case).

Let us illustrate this in the present case. We need first to describe precisely the reconstruction procedure :

(i) Mask 1 can be one of the three solutions (A1), (A2) or (A3) (see figure 8), mask 2 can be one of the three solutions (B1), (B2) or (B3) (see figure 9), and mask 3 one of the six solutions (C1) to (C6) (see figure 10). From these different 2D-masks, we define 2D-functions that are equal to 1 within the open part of the mask (white part on the figures), 0 elsewhere (black part). When choosing the three

masks, we thus define numerically three functions *Mask1(x,y)*, *Mask2(x,z)* and *Mask3(y,z)*. The dimension of these 2D-functions is 150×150 pixels.

(ii) Once three masks have been chosen (for the three views), three matrices are defined as follows :

- These matrices are composed of $150 \times 150 \times 150$ coefficients.
- The coefficients of the first matrix M_1 (linked to view 1 : projection in the plane (X,Y)) are given by : $M_1(x_i, y_j, z_k) = Mask1(x_i, y_j)$,
- The coefficients of the second matrix M_2 (linked to view 2 : projection in the plane (X,Z)) are given by : $M_2(x_i, y_j, z_k) = Mask2(x_i, z_k)$,
- The coefficients of the first matrix M_3 (linked to view 3: projection in the plane (Y,Z)) are given by : $M_3(x_i, y_j, z_k) = Mask3(y_j, z_k)$.

(iii) The reconstructed object is finally described by the new matrix M, composed of $150 \times 150 \times 150$ coefficients given by :

$$M(x_i, y_j, z_k) = M_1(x_i, y_j, z_k) \times M_2(x_i, y_j, z_k) \times M_3(x_i, y_j, z_k)$$

Note that matrix M is not the mathematical product of the three matrices M_1, M_2 and M_3.

(iv) According to the pixel size of figures 8, 9 and 10, each coefficient of the final matrix M represents a voxel of dimensions $31.4 \times 31.4 \times 31.4 \mu m^3$. When the value of a M-coefficient is equal to 1, the particle is composed of this voxel of volume $31.4^3 \mu m^3$. It is possible to estimate the total volume of the reconstructed particle by addition of all coefficients of the final binary matrix M (coefficients equal 1 inside the particle, 0 outside). If we count N non-zero voxels, the volume of the particle is $N \times 31.4^3 \mu m^3$.

(v) From the knowledge of the final matrix M, it is possible to realize back projections of the reconstructed object on the planes (X,Y), (X,Z), and (Y,Z). We can thus obtain the projected shape of the reconstructed particle in these different planes, calculate their respective 2D-autocorrelations and compare them to the original experimental results presented in figures 5(c), 6(c) and 7(c) respectively. This comparison is used to estimate the error of the reconstruction.

Let us now illustrate the reconstruction process in a case where the final reconstructed object does not match the original speckle patterns. The reconstruction is made with the following choice of masks : solution (A1) of figure 8 for view 1 ((X,Y)-plane, function mask1), solution (B3) of figure 9 for view 2 ((X,Z)-plane, function mask2), solution (C1) of figure 10 for view 3 ((Y,Z)-plane, function mask3). Matrix M is then evaluated and we realize a back-projections of the final reconstructed object on planes (X,Y), (X,Z) and (Y,Z). these three back-projections of the reconstructed object are reported on figure 12(a), (b) and (c) respectively. These back-projections are then compared to the original choice of the masks. We thus present on figure 12(d) the difference between the original mask (A1) and the back-projection reported on figure 12(a). The gray part is the domain where there is no difference between both functions. In white (black) is represented the domain where the back-projected face is smaller than the original mask (resp. bigger). No difference is observed on figure 12(d). But the same operation is then done for the views 2 ((X,Z)-plane) and 3 ((Y,Z)-plane). The difference between the backprojected face and the original mask is reported on figure 12(e) and (f) respectively for these two views. It appears on these figures that the final reconstructed object is actually smaller than the initial masks. A conclusion can be drawn : this choice of masks leads to a reconstructed object that is not compatible with the experimental results.

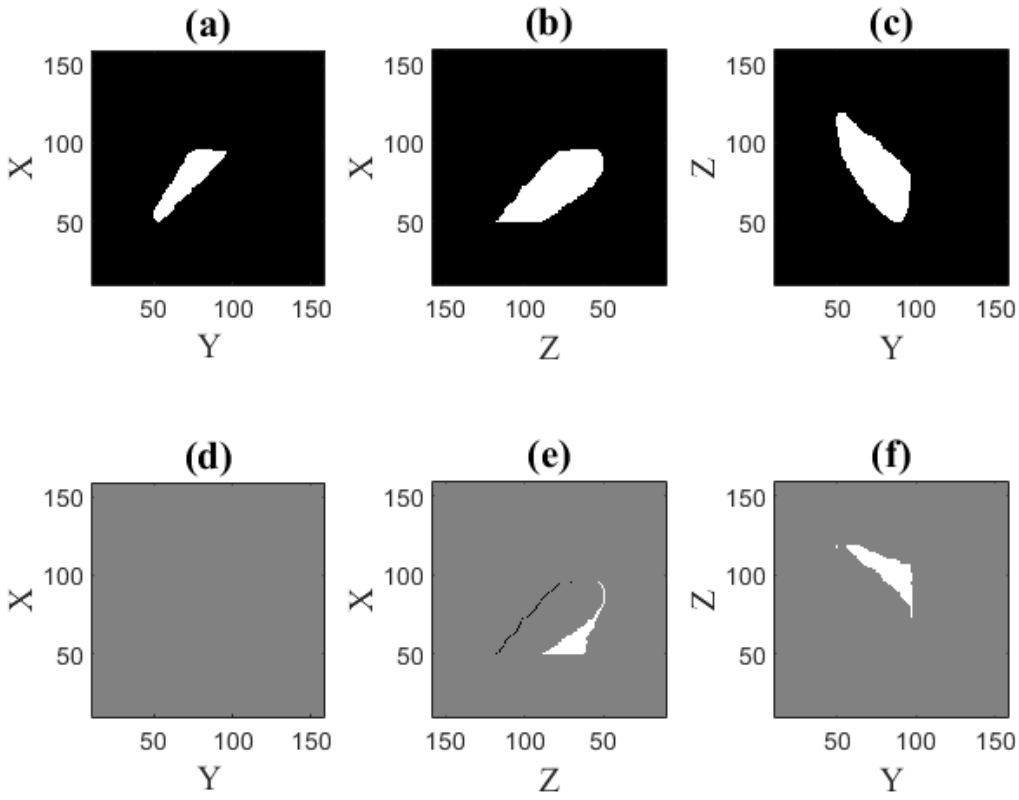

Fig. 12 : the three back-projected faces of the reconstructed object using combination (A1), (B3) and (C1) ((a), (b) and (c) for the three views), and their difference with the expected face ((d), (e) and (f) for the three views respectively) ($31.4\mu m$ per pixel).

Let us consider a second case. The reconstruction is now made with the following choice of masks : solution (A1) of figure 8 for view 1 ((X,Y)-plane, function mask1), solution (B1) of figure 9 for view 2 ((X,Z)-plane, function mask2), solution (C1) of figure 10 for view 3 ((Y,Z)-plane, function mask3). Matrix M is then evaluated and we realize a back-projections of the final reconstructed object on planes (X,Y), (X,Z) and (Y,Z). These back-projections of the reconstructed object are reported on figure 13(a), (b) and (c) respectively. They are then compared to the original masks that have been chosen in this case. Figure 13(d) the difference between the original mask (A1) and the back-projection reported on figure 13(a). The same operation is done for the views 2 ((X,Z)-plane) and 3 ((Y,Z)-plane). The difference between the backprojected face and the original mask is reported on figure 13(e) and (f) respectively for these two views. It appears on these figures that the final reconstructed object corresponds well to all views of the experimental results.

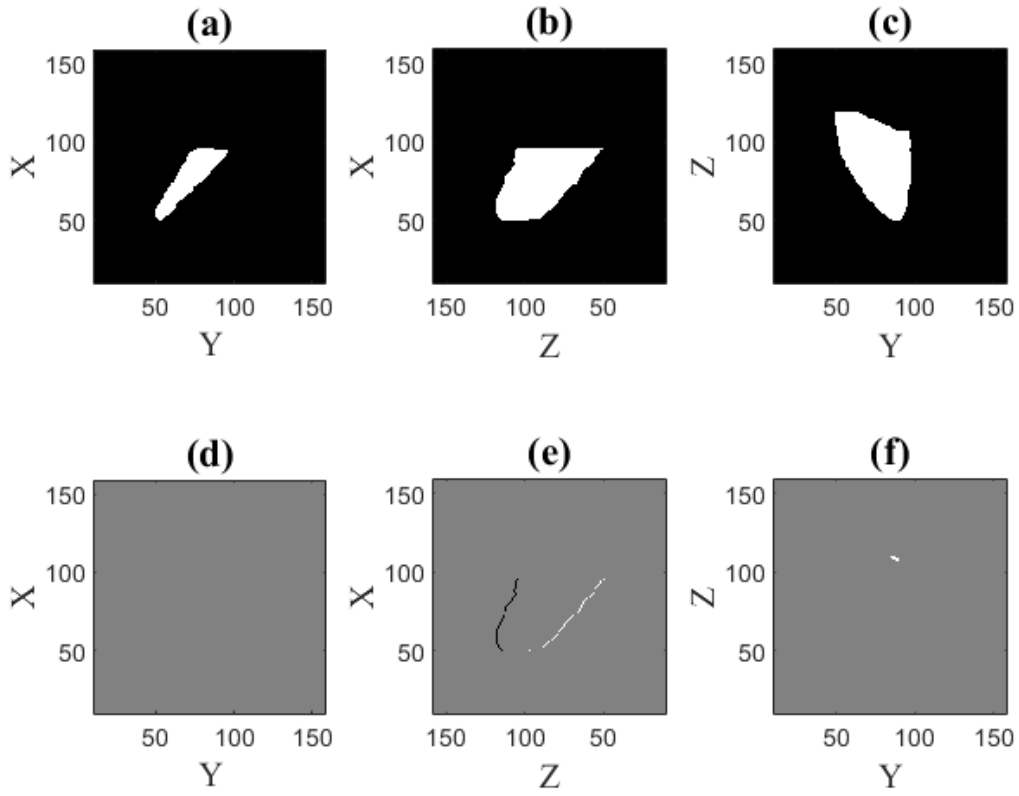

Fig. 13 : the three back-projected faces of the reconstructed object using combination (A1), (B1) and (C1) ((a), (b) and (c) for the three views), and their difference with the expected face ((d), (e) and (f) for the three views respectively) ($31.4\mu m$ per pixel).

Figures 12 and 13 show a way to estimate an error of reconstruction for any combination in the choice of the masks 1, 2 and 3. In both figures 12 and 13, the subfigures (d), (e) and (f) show the difference between the initial mask and the corresponding back-projected face after particle's reconstruction. They are noted $Diff_1(x,y)$, $Diff_2(x,z)$, and $Diff_3(y,z)$ for the three views respectively. These functions equal 0 when there is no difference, +1 or -1 depending on which function is larger. A way to estimate the error of reconstruction is to calculate

$$error = \sum_{(x,y)} |Diff_1(x,y)| + \sum_{(x,z)} |Diff_2(x,z)| + \sum_{(y,z)} |Diff_3(y,Z)|$$

It consists in counting the total number of black and white pixels on subfigures (d), (e) and (f) of figures 12 or 13. It appears clearly that the error will be much bigger in the case of figure 12 than that of figure 13. A second possibility is to calculate in a similar way the difference between the binarized 2D-Fourier transform of the experimental speckle pattern and the binarized 2D-autocorrelation of the back-projected face of the reconstructed particle. This operation is repeated for the three views and the error is evaluated by a summation analog to previous relation (based on the 2D-autocorrelations of the shapes in this second case, and not on the shapes themselves as in the first method). Using this second method, figure 14 shows the error of reconstruction versus the number of the mask's combination. For example the case presented in figure 12 (choice of masks (A1), (B3), (C1)) is the combination's number 3 where the error is very important. The case presented in figure 13 (choice of masks (A1), (B1), (C1)) is the combination's number 1 where the error is the lowest. The combination's number 54 exhibits a very low error factor as well. It corresponds actually to the

choice of masks (A3), (B3) and (C6). It is thus not surprising that combination's numbers 1 and 54 exhibit a similar low error : they represent two centrosymmetric particles.

It is important to keep in mind that this definition of a reconstruction's error does not require the exact knowledge of the shape of the particle. It is indeed deduced from the analysis of the interferometric image (and thus only the experimental data), and its comparison with a reconstructed signal. This is of main importance for the experimenter.

Figure 14 shows finally that we are able to eliminate some 3D-reconstructions that are finally not compatible with the experimental images. But it shows that there is not a single combination with low error. Different combinations of view can indeed exhibit relatively low and comparable errors. Before to conclude, we will try to understand if this elimination of incompatible combinations can present some interest for a more accurate estimation of the volume of the particle.

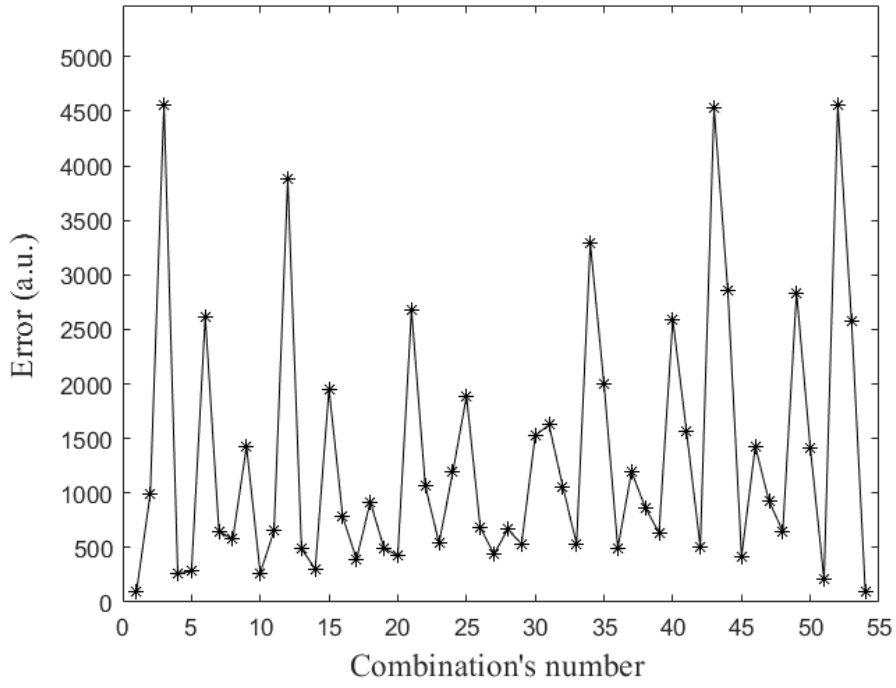

Fig. 14 : experimental error of the reconstruction versus the number of the views' combination

We have already mentioned that the reconstruction process enables an estimation of the volume of the particle. According to the pixel size of figures 8, 9 and 10, each coefficient of the final matrix M represents a voxel of dimensions $31.4^3 \mu m^3$. The total volume of the reconstructed particle is estimated from the addition of all coefficients of matrix M. If we count N non-zero voxels, the volume of the particle is $N \times 31.4^3 \mu m^3$. Figure 15 shows thus the volume of the reconstructed particle for all combinations obtained combining masks (A1) to (A3), (B1) to (B3) and (C1) to (C6). The combination's number is the same as on figure 14. Both figures can thus be compared directly. The volume's unit is the number N of non-zero voxels. We can observe that a few reconstructions induce a lower particle's volume, particularly combination's numbers 3, 12, 21, 34, 43, and 52. It is interesting to note that these cases correspond to combinations where the error is the highest on figure 14. In conclusion, the elimination of incompatible combinations using figure 14 enables the elimination of underestimations of the particle's volume of figure 15. We are not able to identify a

unique combination with the sole figure 14, but we are able to refine the particle's volume estimation by the elimination of the combinations with huge error.

Let us now compare these different values of the particle's volume to the exact one. Experimentally, the particle had been defined by three faces with a random repartition of on-state micromirrors inside 2D-contours for each view, as presented in figure 4. The exact volume of the 3D-object of figure 3 that englobes all these scattering asperities is 40900 voxels, i.e. 1.27mm^3. It is represented by a red line on figure 15. We can see that all values obtained from the different reconstructions are smaller. This is attributed to the low-intensity observed in the corners of the 2D-Fourier transforms of the interferometric patterns. The sharp extremities are eliminated during binarization, as previously mentioned in section IV, and the reconstructed particles are slightly smaller than the original one.

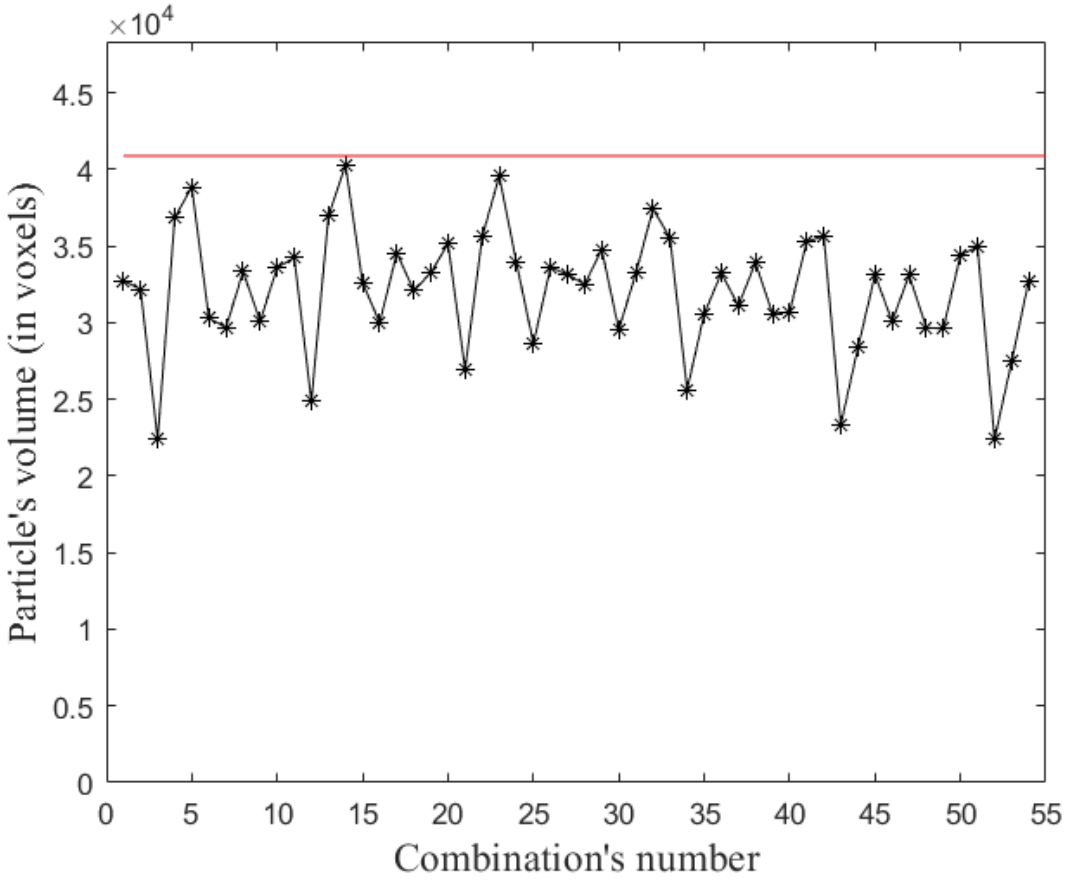

Fig. 15 : volume of the reconstructed particle versus the number of the views' combination (a voxel represents a volume of dimensions $31.4^3 \mu m^3$). The exact volume is given by the plain red line.

VI – Reproducibility of the conclusions

In this last section, we examine a second example in order to know whether the previous conclusions are reproducible with other examples of particles. Figure 16 shows the second particle that will be considered. Its projection in the (X,Y)-plane shows a triangle. We calculate the 2D-autocorrelation of this triangle, and determine a family of possible 2D-shapes whose autocorrelations give the initial one using the trintersection method. Figure 17 shows six possible 2D-shapes whose 2D-autocorrelations match the one of the projection of the particle in the (X,Y)-plane. We can note that the correct shape is the one presented in (A1).

In a similar way, the projection of the particle in the (X,Z)-plane shows an identical triangle. The same figures (A1) to (A6) correspond thus equally to possible 2D-shapes of the projection of the initial particle in the (X,Z) plane (replacing axis-label Y by axis-label Z). It is a deliberate choice in order to reduce the number of figures. Note that the correct shape according to this view is (A1) again.

Finally, for the third view, the basis of this pyramidal particle (its projection in the (Y,Z)-plane) is a square, whose support of the 2D-autocorrelation is a square twice larger. For this view 3, the triintersection method applied to a square gives always a square twice smaller. We will thus consider only one possible 2D-shape.

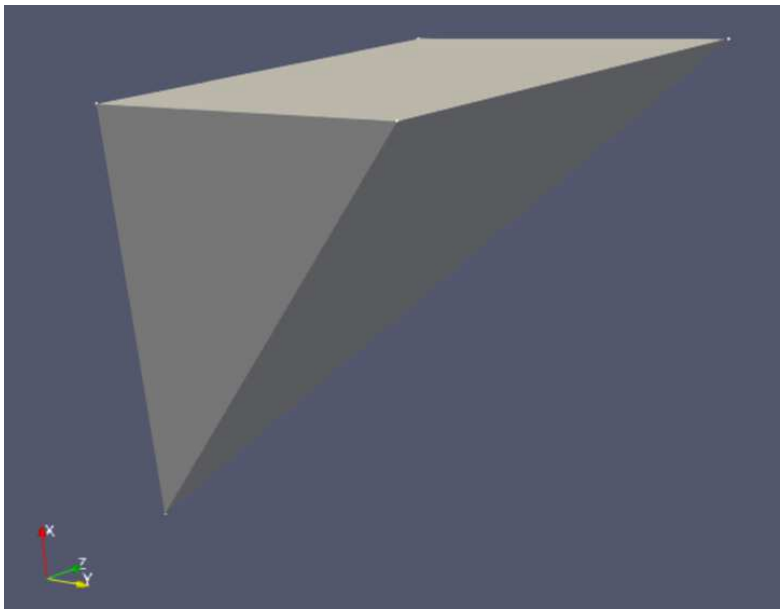

Fig. 16 : 3D-shape of the second particle under study

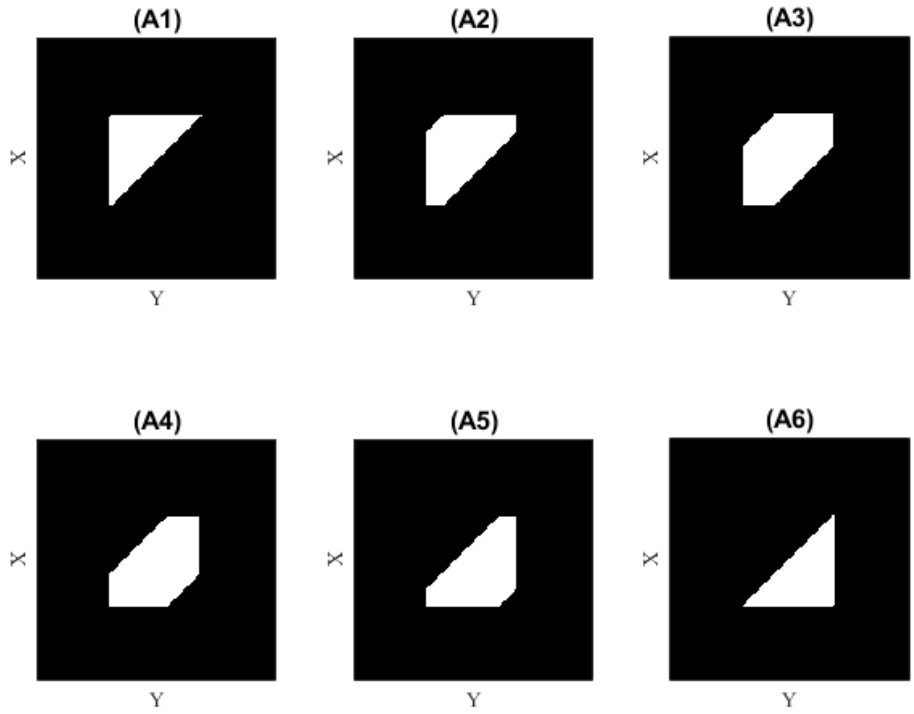

Fig. 17 : six possible 2D-shapes whose 2D-autocorrelations match the one of the projection of particle 2 (Fig. 16) in the (X,Y)-plane.

Combining these different possibilities for the three faces, we can reconstruct $6 \times 6 \times 1 = 36$ possible particles, estimate the error of reconstruction (as previously defined in section V), and calculate the volume of these different possible particles. The results are presented in figure 18. The expected error of the reconstruction versus the combination's number is presented with blue stars with the axis on the left. The expected volume of the reconstructed particle versus the combination's number is presented with red circles with axis on the right. For comparison, the exact volume of the particle is reported as a red line on figure 18. We can draw the following conclusions:

- The lowest error is expected for combination's number 1, i.e. when the 2D-masks in the (X,Z) and in the (X,Y) planes are mask (A1) of figure 17. They correspond to the correct projections.

- A very low error is expected as well for combination's number 36, i.e. when the 2D-masks in the (X,Z) and in the (X,Y) planes are mask (A6) of figure 17. Combination's numbers 1 and 36 correspond actually to two centrosymmetric objects that give the same signatures on the three views. They should exhibit similar errors. The difference is not significant and is just due to numerical error during the calculations.

- A very important error is expected for combination's number 6, i.e. when the 2D-masks in the (X,Z) and in the (X,Y) planes are masks (A1) and (A6) of figure 17 respectively. The 3D-reconstruction in this case leads to a 3D-object that is actually not compatible with the initial projections (as discussed in the case of figure 12).

- The combination's numbers with higher errors are correlated to an underestimation of the particle's volume. The combination of both curves on the same figure enables an elimination of non-compatible 3D-reconstructions with a subsequent better estimation of the particle's volume.

- Different combinations give a low error. In addition, we have limited our analyses to only a few 2D-shapes obtained with the tri-intersection method. When more noise will be present (experimentally for example), we can thus not expect to identify a unique solution with low error. We have observed this experimentally in figure 14 where different combinations give a low error. This conclusion is not so surprising for tomography, keeping in mind that a CT-scan makes the acquisition of many views for proper reconstruction in medical instrumentation. This is complicated here by the fact that the interferometric images give not a 2D-shape but the 2D-autocorrelation of the 2D-shape.

We can thus see with this second example that most of the conclusions already drawn in previous section can still be drawn here.

There is however a significant difference: with the experimental results of the previous sections, the volumes of the possible reconstructed particles were lower than the exact volume : the sharp corners of the particle were indeed smoothed and eliminated during reconstruction from the speckle patterns. In the present section of simulation, the corners are not eliminated. They are taken into account during the reconstruction procedure. The exact volume is not systematically higher than those of the possible reconstructed particles.

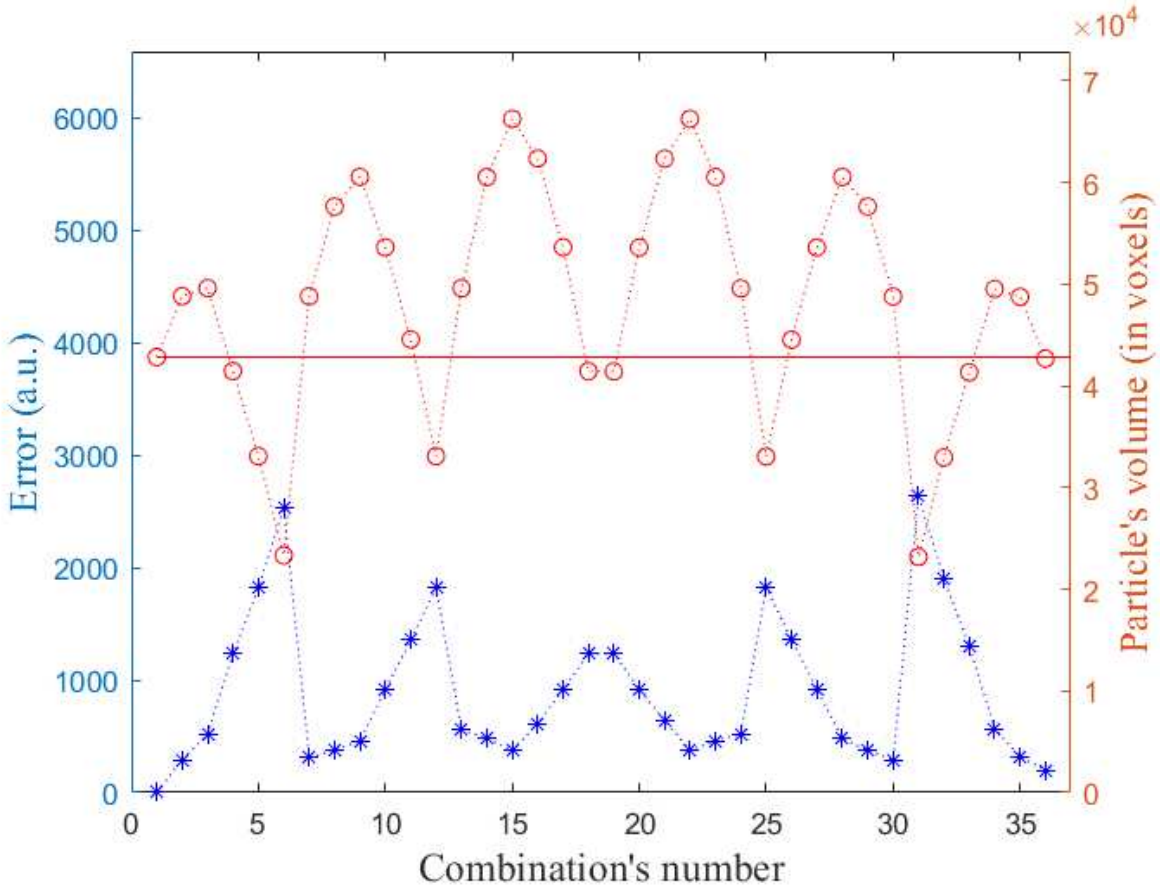

Figure 18: expected error of the reconstruction versus the combination's number (in blue stars, axis on the left); and expected volume of the reconstructed particle versus the combination's number (in red circles, axis on the right). The exact volume is given by the plain red line.

VII – Conclusion

Recent results have shown that the interferometric image of an irregularily-shaped rough particle is directly correlated to the shape of the particle itself. The interferometric image can be analyzed to deliver the 2D-autocorrelation of the contour of the bright part of the particle. Unfortunately, the contour of the 2D-autocorrelation of a 2D-object does not give the contour of the 2D-object itself. The solution is not unique. In the case of multi-view set-ups to realize the tomography of transparent or translucent rough particles in a flow, this multiplicity of solutions adds an important difficulty to reconstruct the 3D-shape of the particles and consequently to estimate the exact volume of the particles. Combining three perpendicular views, we have seen that it is possible to reconstruct a family of possible 3D-shapes. For each of them, an estimation of the volume of the particle can be done. It is possible to identify 3D-reconstructions that are not compatible with the three views. The estimation of an error parameter enables to eliminate some 3D-shapes, and to obtain more accurate estimation of the particle's volume. In the cases that have been studied, the lowest error gives the best approaching faces for the three views of observation. Nevertheless, other 3D-shapes corresponding to a deformation of the initial particle can give a quite similar error. Relation (1) links both functions $|\mathrm{FT_{2D}[I]}(\lambda\,\mathrm{B_{tot}}\,u, \lambda\,\mathrm{B_{tot}}\,v)|$ and $|\mathrm{A_{2D}[G_0]}(dx, dy)|$ in any point ($\lambda\,\mathrm{B_{tot}}\,u, \lambda\,\mathrm{B_{tot}}\,v$) and (dx,dy) respectively. Experimentally, the use of this approached relation has been limited to the comparison of the contours of both binarized functions. If the relation between both functions could be validated experimentally in any point, other image processing tools should enable a more precise identification of the exact shape of the particle [18]. Experimental demonstrations are thus to be done in this direction. Combined with deep learning approaches, these techniques should deliver new methods of particle characterization [19]. These recent studies offer very interesting perspectives for the 3D-characterization of particles in cloud chambers or clouds during airborne operations [20,21].

Acknowledgment

Authors thank Région Normandy for CPER and European Union for FEDER project "THESIS".

References

[1] F. Joachim, (ed.) Electron Tomography: Methods for Three-Dimensional Visualization of Structures in the Cell, 2nd ed., (Springer, New York, 2006).

[2] A. J. Koster, U. Ziese, A. J. Verkleij, A. H. Janssen, and K. P. de Jong, Three-dimensional transmission electron microscopy: A novel imaging and characterization technique with nanometer scale resolution for material science, J. Phys. Chem. B 104 (2000) 9368–9370.

[3] D. Jin, R. Zhou, Z. Yaqoob, and P. T. C. So, Tomographic phase microscopy: Principles and applications in Bioimaging, J. Opt. Soc. Am. B 34 (2017) B64–B77.

[4] F. Merola, P. Memmolo, L. Miccio, M. Mugnano, and P. Ferraro, Phase contrast tomography at lab on chip scale by digital holography, Methods 136 (2018) 108–115.

[5] Y.-L. Pan, C. Wang, S. C. Hill, M. Coleman, L. A. Beresnev, and J. L. Santarpia, Trapping of individual airborne

absorbing particles using a counterflow nozzle and photophoretic trap for continuous sampling and analysis, Appl. Phys. Lett. 104 (2014) 113507.
[6] J. C. Laning and M. J. Berg, Orthographic imaging of free-flowing aerosol particles, OSA Continuum 2 (2019) 3514-3520.
[7] M. Brunel, B. Delestre, and M. Talbi, 3D-reconstructions for the estimation of ice particle's volume using a two-views interferometric out-of-focus imaging set-up, Rev. Sci. Instrum. 90 (2019) 053109.
[8] M. Brunel, S. González Ruiz, J. Jacquot, and J. van Beeck, On the morphology of irregular rough particles from the analysis of speckle like interferometric out-of-focus images, Opt. Commun. 338 (2015) 193–198.
[9] L. Ouldarbi, M. Talbi, S. Coëtmellec, D. Lebrun, G. Gréhan, G. Perret, and M. Brunel, 3D-shape recognition and size measurement of irregular rough particles using multi-views interferometric out-of-focus imaging, Appl. Opt. 55 (2016) 9154–9159.
[10] J. Jacquot-Kielar, P. Lemaitre, C. Gobin, Y. Wu, E. Porcheron, S. Coetmellec, G. Gréhan, and M. Brunel, Simultaneous interferometric in-focus and out-of-focus imaging of ice crystals, Opt. Commun. 372 (2016) 185–195.
[11] S. G. Ruiz and J. van Beeck, Sizing of sand and ash particles using their speckle pattern: influence of particle opacity, Exp. Fluids 58 (2017) 100–108.
[12] M. Talbi, G. Gréhan and M. Brunel, Interferometric particle imaging of ice particles using a multi-view optical system, Appl. Opt. 57 (2018) 6188-6197.
[13] J. Sun, H. Zhang, Z. Li, D. Jia, T. Liu and M. Zhai, Determining speckle orientation of interferometric out-of-focus images, J. Quant. Spectrosc. Radiat. Transfer 226 (2019) 73-80.
[14] X. Wu, L. Shi, Z. Lin, Y. Wu, M. Brunel, J. Jacquot, and G. Gréhan, Dual-beam interferometric particle imaging for size and shape characterization of irregular coal micro-particle: validation with digital inline holography, J. Quantum Spectrosc. Radiat. Transfer 241 (2020) 106728.
[15] M. Fromager, K. Aït Ameur, M. Brunel, Digital micromirror device as programmable rough particle in interferometric particle imaging, Appl. Opt. 56 (2017) 3594-3598.
[16] M. Talbi, M. Fromager, F. Corbin, M. Brunel, Interferometric images of irregular rough particles in presence of time-dependent index inhomogeneities in front of the imaging system, Appl. Opt. 58 (2019) 5865-5872.
[17] R. Fienup, T.R. Crimmins and W. Holsztynski, Reconstruction of the support of an object fro the support of its autocorrelation, J. Opt. Soc. Am. 7 (1982) 3-13.
[18] H. Shen, L. Wu, Y. Li and W. Wang, Two-dimensional shape retrieval from the interferometric out-of-focus image of a nonspherical particle – Part I:theory, Appl. Opt. 57 (2018) 4968-4976.
[19] P. Piedra, A. Kalume, E. Zubko, D. Mackowski, Y. Le Pan, and G. Videen, Particle-shape classification using light scattering: An exercise in deep learning, J. Quantum Spectrosc. Radiat. Transfer 231 (2019) 140-156.
[20] J. Sun, Z. Li, P. Tian, R. Li, D. Jia, T. Liu, and H. Zhang, Measurement of cloud particles in a cloud chamber based on interference technology, Appl. Opt. 58 (2019) 8757-8764.
[21] E. Porcheron, P. Lemaitre, J. van Beeck, R. Vetrano, M. Brunel, G. Gréhan, and L. Guiraud, Development of a spectrometer for the airborne measurement of droplet sizes in clouds, J. Eur. Opt. Soc. 10 (2015) 15030.